

# Graphene oxide-decorated $\text{Fe}_2(\text{MoO}_4)_3$ microflowers as a promising anode for lithium and sodium storage

Chunhua Han<sup>1</sup> (✉), Xiaoji Ren<sup>1</sup>, Qidong Li<sup>1</sup>, Wen Luo<sup>1,2</sup>, Lei Huang<sup>1</sup>, Liang Zhou<sup>1</sup>, and Liqiang Mai<sup>1,†</sup> (✉)

<sup>1</sup> State Key Laboratory of Advanced Technology for Materials Synthesis and Processing, Wuhan University of Technology, Luoshi Road 122, Wuhan 430070, China

<sup>2</sup> Laboratoire de Chimie et Physique: Approche Multiéchelles des Milieux Complexes, Institut Jean Barriol, Université de Lorraine, 57070 Metz, France

<sup>†</sup> Present address: Department of Chemistry, University of California, Berkeley, California 94720, USA

Received: 19 April 2017

Revised: 11 June 2017

Accepted: 23 June 2017

© Tsinghua University Press  
and Springer-Verlag GmbH  
Germany 2017

## KEYWORDS

$\text{Fe}_2(\text{MoO}_4)_3$  microflowers,  
anode,  
lithium and sodium storage

## ABSTRACT

Mixed transition metal oxides (MTMOs) have received intensive attention as promising anode materials for lithium-ion batteries (LIBs) and sodium-ion batteries (SIBs). In this work, we demonstrate a facile one-step water-bath method for the preparation of graphene oxide (GO) decorated  $\text{Fe}_2(\text{MoO}_4)_3$  (FMO) microflower composite (FMO/GO), in which the FMO is constructed by numerous nanosheets. The resulting FMO/GO exhibits excellent electrochemical performances in both LIBs and SIBs. As the anode material for LIBs, the FMO/GO delivers a high capacity of  $1,220 \text{ mAh}\cdot\text{g}^{-1}$  at  $200 \text{ mA}\cdot\text{g}^{-1}$  after 50 cycles and a capacity of  $685 \text{ mAh}\cdot\text{g}^{-1}$  at a high current density of  $10 \text{ A}\cdot\text{g}^{-1}$ . As the anode material for SIBs, the FMO/GO shows an initial discharge capacity of  $571 \text{ mAh}\cdot\text{g}^{-1}$  at  $100 \text{ mA}\cdot\text{g}^{-1}$ , maintaining a discharge capacity of  $307 \text{ mAh}\cdot\text{g}^{-1}$  after 100 cycles. The promising performance is attributed to the good electrical transport from the intimate contact between FMO and graphene oxide. This work indicates that the FMO/GO composite is a promising anode for high-performance lithium and sodium storage.

## 1 Introduction

The high consumption of fossil fuels has stimulated increasing demand for renewable energy resources, as well as advanced energy storage systems. Lithium-ion batteries (LIBs), which have been extensively employed in portable electronics and electric vehicles, are regarded as attractive energy storage devices because

of their high energy density and long cycling life [1–8]. Recently, sodium-ion batteries (SIBs) have also received much attention because of the abundant sodium resources, which can reduce the cost of batteries for large-scale energy storage applications [9–14]. Graphite, as the anode material of commercialized LIBs, delivers a capacity of only  $372 \text{ mAh}\cdot\text{g}^{-1}$  [15]. Moreover, it shows poor sodium-storage performance [16]. Therefore, the

Address correspondence to Liqiang Mai, mlq518@whut.edu.cn; Chunhua Han, hch5927@whut.edu.cn

development of high-performance anode materials for LIBs and SIBs is an important topic.

Among the numerous anode candidates, mixed transition metal oxides (MTMOs), for example, manganates, ferrites and molybdates, exhibit excellent electrochemical properties due to their relatively higher electrical conductivity [17]. Transition metal molybdates, such as  $\text{Fe}_2(\text{MoO}_4)_3$  [18],  $\text{NiMoO}_4$  [19],  $\text{CoMoO}_4$  [20], and  $\text{MnMoO}_4$  [21], have received intensive interest as the anode for lithium storage, owing to their high capacity, low cost, eco-friendliness and the rich oxidation states of molybdenum. For instance, Wang et al. [19] synthesized  $\text{NiMoO}_4$  nanosheets on a graphene network, which exhibited a capacity retention of 89% after 120 cycles at  $200 \text{ mA}\cdot\text{g}^{-1}$ . Yao et al. [20] prepared  $\text{CoMoO}_4$  nanoparticles/reduced graphene oxide, which showed impressive cycling stability and rate performance because of their synergistic effect and the crystal structure of  $\text{CoMoO}_4$ . However, to date, there have been few investigations on the electrochemical sodium-storage performance of molybdates. Chen et al. [22] reported an  $\text{Ag}_2\text{Mo}_2\text{O}_7$  anode with good rate capability and long-term cycling life. Nevertheless, the transition metal molybdates usually suffer from problems, which include large volume changes, as well as relatively low conductivity. Tremendous efforts have been devoted to relieving these issues by combining molybdates with various carbon materials, for example carbon nanotubes and (reduced) graphene oxide nanosheets [18, 20, 21, 23, 24]. Among them, (reduced) graphene oxide nanosheets have been demonstrated to be an excellent conductive network, as well as elastic buffering layer, which can accommodate the volume expansion in electrochemical processes [20, 23].

In this work, we synthesized graphene oxide-decorated  $\text{Fe}_2(\text{MoO}_4)_3$  microflower composite (FMO/GO) via a facile one-step water-bath method. The as-prepared FMO/GO demonstrated high specific capacity ( $1,200 \text{ mAh}\cdot\text{g}^{-1}$  at  $100 \text{ mA}\cdot\text{g}^{-1}$ ) and impressive rate capability ( $685 \text{ mAh}\cdot\text{g}^{-1}$  at  $10 \text{ A}\cdot\text{g}^{-1}$ ) in lithium storage. The sodium-storage performance of FMO/GO as an anode has been studied for the first time; it manifests excellent cycling performance ( $\sim 188 \text{ mAh}\cdot\text{g}^{-1}$  after 1,000 cycles at  $1 \text{ A}\cdot\text{g}^{-1}$ ) and rate capability

( $107 \text{ mAh}\cdot\text{g}^{-1}$  at  $10 \text{ A}\cdot\text{g}^{-1}$ ). The enhanced electrochemical properties can be attributed to the combination of  $\text{Fe}_2(\text{MoO}_4)_3$  microflowers and conductive graphene oxide, which provides a pathway for electron transport and buffers the volume changes during the discharge/charge processes.

## 2 Experimental

### 2.1 Material preparation

The FMO/GO was synthesized by a facile one-step water-bath method. In a typical synthesis, 1 mL of GO (1.01 wt.%) was dispersed in 10 mL of deionized water by ultrasonication for half an hour.  $(\text{NH}_4)_6\text{Mo}_7\text{O}_{24}\cdot 4\text{H}_2\text{O}$  (0.265 g) was dissolved in 10 mL of deionized water and added to the GO suspension, followed by stirring at  $80^\circ\text{C}$  in a water bath. Then, 10 mL of deionized water containing 0.404 g of  $\text{Fe}(\text{NO}_3)_3\cdot 9\text{H}_2\text{O}$  was added dropwise to the GO suspension. The resulting solution was stirred at  $80^\circ\text{C}$  for 12 h. The final product was washed several times with deionized water and ethanol, and then dispersed in 10 mL deionized water. After freeze-drying, the FMO/GO was obtained. The pristine FMO was prepared via the same method without adding GO.

### 2.2 Materials characterization

X-ray diffraction (XRD) experiments were carried out to investigate the phase and crystal information using a Bruker D8 Advance X-ray diffractometer with a non-monochromated  $\text{Cu K}\alpha$  X-ray source. Scanning electron microscopy (SEM) images and energy-dispersive X-ray spectra (EDS) were obtained with a JEOL-7100F microscope operated at an acceleration voltage of 10 kV. Transmission electron microscopy (TEM) and high-resolution TEM (HRTEM) images were collected using a JEM-2100F microscope. X-ray photoelectron spectroscopy (XPS) measurements were acquired with a VG Multi Lab 2000 instrument. The content of graphene oxide in the sample was confirmed by using a Netzsch STA 449 C simultaneous thermal analyzer at a heating rate  $10^\circ\text{C}\cdot\text{min}^{-1}$  in air. Raman measurements were performed with a Renishaw RM-1000 laser Raman microscope.

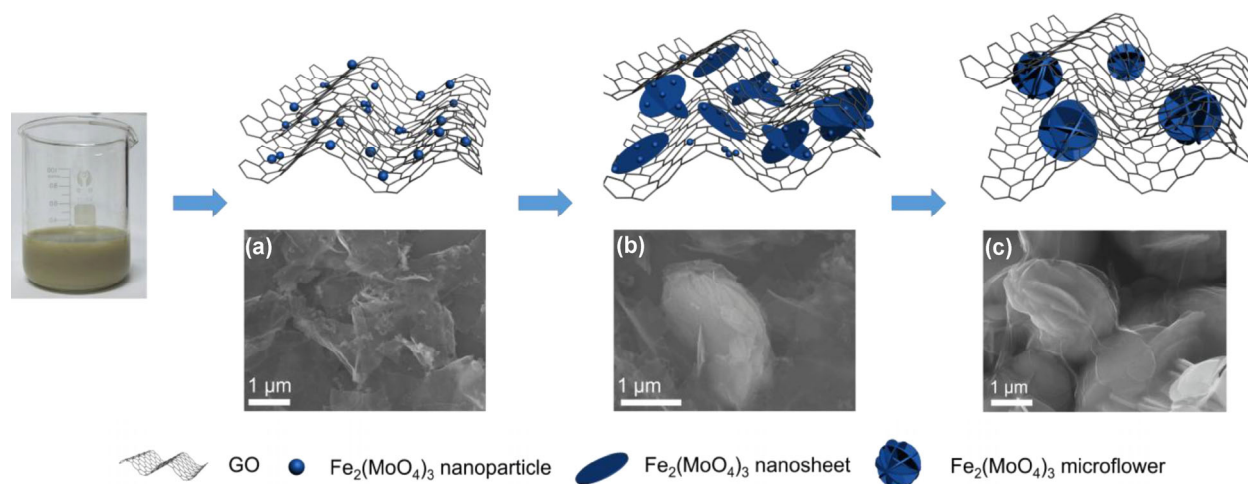
### 2.3 Measurement of electrochemical performance

The electrochemical properties of LIBs and SIBs were measured by assembling 2016 coin cells in a glove box filled with argon. The working electrodes were prepared by mixing the active material, acetylene black and carboxyl methyl cellulose at a weight ratio of 80:15:5. The slurry was pasted on an aluminum foil for SIBs and a titanium foil for LIBs, then dried at 100 °C for 6 h in a vacuum oven. The mass loading of active material was  $\sim 1.0 \text{ mg}\cdot\text{cm}^{-2}$ . In sodium half cells, sodium was used as the counter electrode, and 1 M  $\text{NaClO}_4$  in ethylene carbonate (EC)/dimethyl carbonate (DMC) (EC:DMC = 1:1, by weight) with 5 wt.% fluoroethylene carbonate (FEC) was used as the electrolyte. A glass fiber membrane (GF/D, Whatman) was used as the separator. For the lithium half cells, metallic lithium was used as the counter electrode and the electrolyte consisting of 1 M  $\text{LiPF}_6$  dissolved in EC/DMC with a volumetric ratio of 1:1. The galvanostatic discharge/charge measurements were investigated in a voltage range of 0.01–3 V with a multi-channel battery testing system (LAND CT2001A). Cyclic voltammetry (CV) curves were collected at room temperature (25 °C) using an Autolab potentiostat/galvanostat (Autolab PGSTAT 302). Electrochemical impedance spectroscopy (EIS) measurements were performed with an Autolab Potentiostat Galvanostat. EIS was measured under open-circuit potential before cycling in a frequency range of  $10^{-2}$ – $10^5$  Hz.

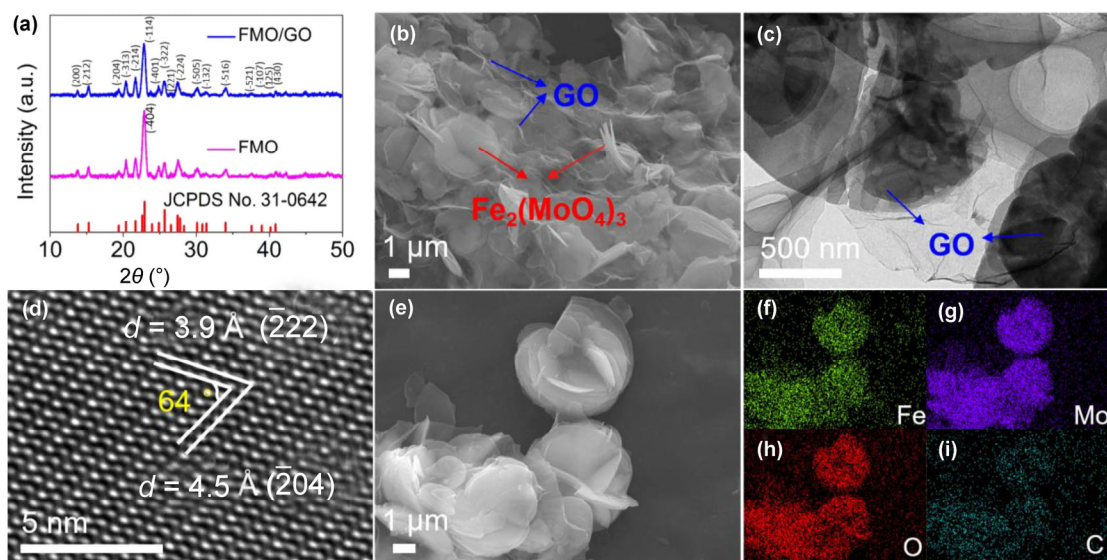
### 3 Results and discussion

Figure 1 depicts the growth process of FMO/GO. First,  $\text{Fe}^{3+}$  was absorbed by the GO due to the presence of functional groups [24]. The  $\text{Mo}_7\text{O}_{24}^{6-}$  was then attracted by  $\text{Fe}^{3+}$  to form  $\text{Fe}_2(\text{MoO}_4)_3$  crystal nuclei on the GO surface. As the reactions proceeded, the FMO crystal nuclei grew into nanoparticles (Fig. 1(a)), followed by transformation into nanosheets (Fig. 1(b)), and eventually microflowers (Fig. 1(c)).

Figure 2(a) shows the XRD patterns of the as-prepared FMO and FMO/GO. It can be observed that all the diffraction peaks in both patterns are well indexed to monoclinic  $\text{Fe}_2(\text{MoO}_4)_3$  (JCPDS card No. 31-0642), suggesting the samples are highly pure. To verify the existence of GO in FMO/GO, Raman spectroscopy measurements were carried out. Two broad peaks can be observed at 1,344 and 1,605  $\text{cm}^{-1}$  in the Raman spectrum of FMO/GO (Fig. S1 in the Electronic Supplementary Material (ESM)), which are ascribed to the D-band and G-band of GO, respectively [25]. Thermogravimetric analysis (TGA) was used to investigate the GO content in FMO/GO (Fig. S2 in the ESM). The mass loss of the first step between 40 and 250 °C is 3.4 wt.%, which is ascribed to the removal of adsorbed water and crystal water. The mass loss from 250 to 600 °C is attributed to GO oxidation, and the GO content of FMO/GO is approximately 1.4 wt.%. Figure 2(b) and Fig. S3 in the ESM display the SEM images of FMO/GO, which show that the  $\text{Fe}_2(\text{MoO}_4)_3$



**Figure 1** Schematic illustration of FMO/GO formation. SEM images of FMO/GO at various reaction time: (a) 2 h; (b) 6 h; (c) 12 h.



**Figure 2** (a) XRD patterns of FMO and FMO/GO; (b) SEM, (c) TEM, and (d) HRTEM images of FMO/GO; (e)–(i) EDS mapping images of FMO/GO.

microflowers constructed by numerous nanosheets are uniformly embedded in a GO network. The FMO/GO composite structure can be further confirmed by the TEM image (Fig. 2(c)). It has been reported that such three-dimensional (3D) structures can effectively prevent nanosheets aggregation, and act as a stress buffer during cycling, consequently enhancing electrochemical performance [26]. Figure 2(d) exhibits two sets of lattice fringes, and the lattice spacings of 3.9 and 4.5 Å correspond with the  $(\bar{2}22)$  and  $(\bar{2}04)$  planes of  $\text{Fe}_2(\text{MoO}_4)_3$ , respectively. The angle between these two planes is 64°, which agrees with the theoretical value. The EDS mapping (Figs. 2(e)–2(i)) of FMO/GO shows that the Fe, Mo, O, and C elements are uniformly distributed. SEM and TEM images of the pristine FMO are presented in Fig. S4 in the ESM. It consists of microflowers with nanosheet building blocks. The thickness of the primary nanosheets is ~100 nm.

Figure 3 shows the electrochemical performance of FMO and FMO/GO in lithium-ion half cells. To investigate the electrochemical behavior of FMO/GO, CV tests were performed in the potential window of 0.01–3 V vs.  $\text{Li}^+/\text{Li}$  at a scan rate of 0.1  $\text{mV}\cdot\text{s}^{-1}$ . As shown in Fig. 3(a), three reduction peaks are detected in the initial cycle. The peak centered at 2.95 V is attributed to the insertion of  $\text{Li}^+$  into the  $\text{Fe}_2(\text{MoO}_4)_3$

lattice [27]. The other two peaks located at 1.45 and 0.30 V are due to the complete reduction of  $\text{Mo}^{6+}$  to  $\text{Mo}^0$ , and  $\text{Fe}^{3+}$  to  $\text{Fe}^0$ , as well as the formation of a solid-electrolyte interphase (SEI) layer [28]. Two anodic peaks can be observed at 1.44 and 1.8 V. The first peak is assigned to the oxidation of  $\text{Mo}^0$  to  $\text{Mo}^{4+}$ , while the second peak is due to the oxidation of  $\text{Mo}^{4+}$  to  $\text{Mo}^{6+}$ , as well as the oxidation of  $\text{Fe}^0$  to  $\text{Fe}^{3+}$  [24, 29]. The cathodic peaks appeared in the second and third cycles, and are observed at 1.55, 0.66, and 0.15 V, corresponding to the reduction of  $\text{Mo}^{6+}$  to  $\text{Mo}^{4+}$ ,  $\text{Fe}^{3+}$  to  $\text{Fe}^0$ , and  $\text{Mo}^{4+}$  to  $\text{Mo}^0$ , respectively [24, 29]. The discharge/charge curves of FMO/GO in the voltage range of 0.01–3 V vs.  $\text{Li}^+/\text{Li}$  at a current density of 200  $\text{mA}\cdot\text{g}^{-1}$  are displayed in Fig. 3(b). The initial discharge and charge capacities are 1,406 and 1,150  $\text{mAh}\cdot\text{g}^{-1}$ , respectively, and the initial Coulombic efficiency is nearly 82%. Moreover, the subsequent discharge and charge curves exhibit almost no change, demonstrating the good reversibility of FMO/GO. The initial capacity loss commonly results from SEI layer formation [20]. Figure 3(c) depicts the cycling performances of the pristine FMO and FMO/GO at 200  $\text{mA}\cdot\text{g}^{-1}$ . After 50 cycles, the FMO/GO and pristine FMO retain 1,220 and 855  $\text{mAh}\cdot\text{g}^{-1}$ , respectively, revealing the better cycling stability of FMO/GO. Rate capabilities of the as-synthesized two samples were

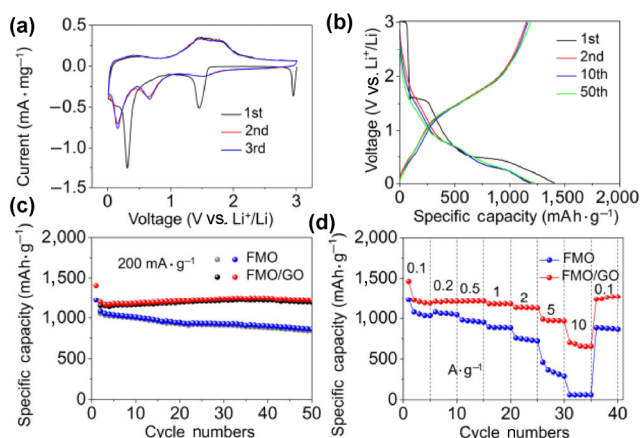


**Figure 3** Electrochemical performance of FMO and FMO/GO in lithium storage. (a) CV curves of FMO/GO at a scan rate of  $0.1 \text{ mV}\cdot\text{s}^{-1}$  from 0.01 to 3 V; (b) discharge/charge profiles of FMO/GO at  $200 \text{ mA g}^{-1}$ ; (c) cycling performances of FMO and FMO/GO at  $200 \text{ mA}\cdot\text{g}^{-1}$ ; (d) rate capabilities of FMO and FMO/GO.

further explored (Fig. 3(d)). The FMO/GO demonstrates discharge capacities of 1,200, 1,205, 1,209, 1,176, 1,130, 970, and  $685 \text{ mAh}\cdot\text{g}^{-1}$  at current densities of 0.1, 0.2, 0.5, 1, 2, 5, and  $10 \text{ A}\cdot\text{g}^{-1}$ , respectively. Furthermore, the discharge capacity can be restored to  $1,260 \text{ mAh}\cdot\text{g}^{-1}$  when the current density returns to  $0.1 \text{ A}\cdot\text{g}^{-1}$ , indicating excellent reversibility of the electrode material. Surprisingly, the capacity increases slightly with an increase in current density from 0.1 to  $0.5 \text{ A}\cdot\text{g}^{-1}$ , which is attributed to the activation process. A similar activation process has been reported in many other transition metal oxide-based anode materials [30–32]. In comparison, the FMO exhibits a capacity below  $50 \text{ mAh}\cdot\text{g}^{-1}$  at  $10 \text{ A}\cdot\text{g}^{-1}$ , and the capacity cannot be recovered to its initial value when the current density returns to  $0.1 \text{ A}\cdot\text{g}^{-1}$ . The long-term cycling performance of FMO/GO at  $1 \text{ A}\cdot\text{g}^{-1}$  was also investigated (Fig. S5 in the ESM). A capacity of  $\sim 480 \text{ mAh}\cdot\text{g}^{-1}$  is retained after 500 cycles. Remarkably, the FMO/GO delivers higher capacity and better rate performance than other transition metal molybdates reported previously in the literatures (Table S1 in the ESM). The excellent electrochemical performance of FMO/GO indicates that the GO and 3D microflower structure can improve electrical/ionic transport in the electrode, which leads to fast electrochemical kinetics. The enhanced electronic conductivity can be confirmed by the Nyquist plots

(Fig. S6 in the ESM), which shows charge-transfer resistance values of 174 and  $304 \Omega$  for FMO/GO and FMO, respectively.

The sodium-storage performances of the as-prepared samples were also evaluated. Figure 4(a) shows the CV curves of FMO/GO in the potential range of 0.01–3 V vs.  $\text{Na}^+/\text{Na}$ , at a scan rate of  $0.1 \text{ mV}\cdot\text{s}^{-1}$ . The differences in electrochemical behavior between SIBs and LIBs are partly attributed to the more sluggish sodium insertion and extraction kinetics owing to the larger sodium-ion radius. Figures 4(b) and 4(c) present the discharge/charge profiles of FMO/GO and the cycling performances of both samples at  $100 \text{ mA}\cdot\text{g}^{-1}$ . The first discharge and charge capacities of FMO/GO are  $571$  and  $448 \text{ mAh}\cdot\text{g}^{-1}$ , respectively, and the initial Coulombic efficiency is 78%. The irreversible capacity loss is due to SEI film formation [13]. The capacity of FMO/GO decays from 571 to  $340 \text{ mAh}\cdot\text{g}^{-1}$  in the initial 20 cycles and remains stable in the following cycles, showing enhanced cycling stability. For both samples, the initial discharge capacities in sodium storage are much lower than those in lithium storage, which is due to the lower reaction depth caused by the more sluggish kinetics and the higher standard electrode potential of  $\text{Na}^+/\text{Na}$  compared to that of  $\text{Li}^+/\text{Li}$  ( $-2.71$  and  $-3.04 \text{ V}$  (vs. standard hydrogen electrode (SHE)), respectively) [33]. In comparison, FMO delivers a lower discharge capacity of  $496 \text{ mAh}\cdot\text{g}^{-1}$ , and only  $156 \text{ mAh}\cdot\text{g}^{-1}$  is retained after 100 cycles. The rate capabilities of both samples were also evaluated (Fig. 4(d)). The FMO/GO delivers average discharge capacities of 411, 348, 293, 264, 227, 169, and  $107 \text{ mAh}\cdot\text{g}^{-1}$  at current densities of 0.1, 0.2, 0.5, 1, 2, 5, and  $10 \text{ A}\cdot\text{g}^{-1}$ , respectively. Furthermore, the discharge capacity can be restored to  $302 \text{ mAh}\cdot\text{g}^{-1}$  when the current density returns to  $0.1 \text{ A}\cdot\text{g}^{-1}$ , indicating relatively good reversibility of the electrode material. In sharp contrast, the discharge capacity of FMO fades to 0 at  $10 \text{ A}\cdot\text{g}^{-1}$ . The long-term cycling performance of FMO/GO at  $1 \text{ A}\cdot\text{g}^{-1}$  was investigated (Fig. 4(e)). A capacity of  $188 \text{ mAh}\cdot\text{g}^{-1}$  is maintained after 1,000 cycles, and the capacity loss is around 0.048% per cycle. The FMO/GO shows better rate performance than many of the other transition metal molybdates reported previously in the literatures (Table S2 in the ESM). The enhanced sodium-storage performance of FMO/GO can be

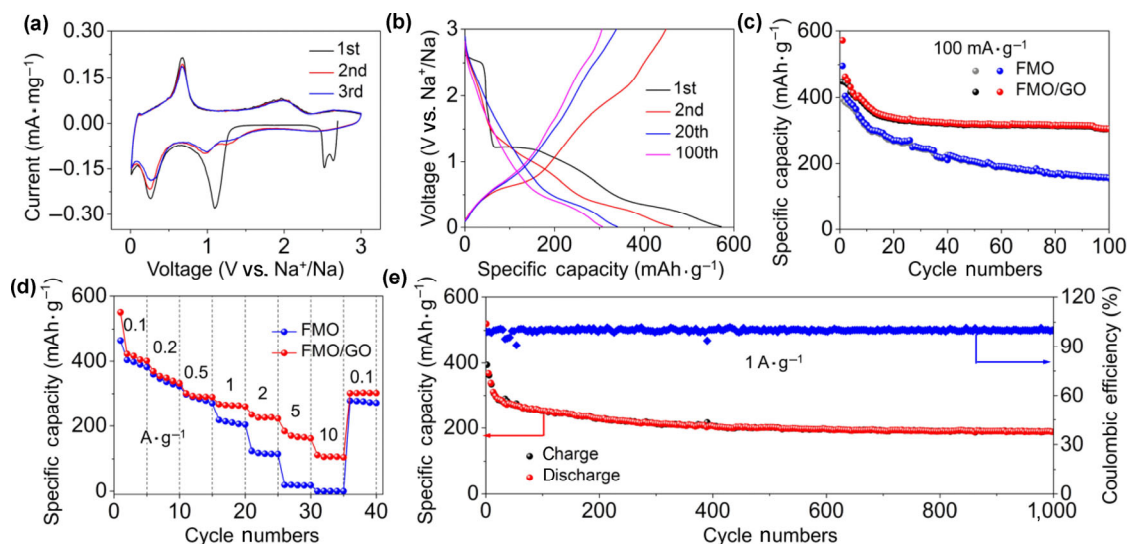


**Figure 4** Electrochemical performance of FMO and FMO/GO in sodium storage. (a) CV curves of FMO/GO at a scan rate of  $0.1 \text{ mV}\cdot\text{s}^{-1}$  from 0.01 to 3 V; (b) discharge/charge curves of FMO/GO at  $100 \text{ mA}\cdot\text{g}^{-1}$ ; (c) cycling performances of FMO and FMO/GO at  $100 \text{ mA}\cdot\text{g}^{-1}$ ; (d) rate performances of FMO and FMO/GO; (e) long-term cycling performance of FMO/GO at  $1 \text{ A}\cdot\text{g}^{-1}$ .

ascribed to GO, which improves the electrical conductivity of the electrode (Fig. S7 in the ESM) and effectively stops aggregation and pulverization of the active materials (Fig. S8 in the ESM).

We also investigated the sodium-storage mechanism of FMO by *ex-situ* XRD and TEM measurements of the fully sodiated/de-sodiated states. When discharged to 0.01 V, both  $\text{Na}_{2+x}\text{MoO}_{4-\delta}$  and Fe can be detected (Figs. 5(a)–5(c)). When re-charged to 3 V, the diffraction peaks/rings for both  $\text{Na}_{2+x}\text{MoO}_{4-\delta}$  and Fe disappear, and an entirely amorphous product is obtained (Figs. 5(a), 5(d), and 5(e)). To further confirm the sodium-storage mechanism, XPS measurements of the fully sodiated/de-sodiated states were also carried out, as shown in

Fig. S9 in the ESM. When discharged to 0.01 V, the peaks located at 706.3 and 719.4 eV (Fig. S9(a) in the ESM) are attributed to  $\text{Fe}^0$  [34], which is consistent with the SAED analysis in Fig. 5(c). The peaks centered at 710.2 and 723.3 eV correspond to  $\text{Fe}^{2+}$  [35], which is possibly due to the surface oxidation of Fe nanoparticles. The Mo 3d peaks are displayed in Fig. S9(b) in the ESM. The peaks at 228.7, 231.8, 232, and 235.1 eV are ascribed to Mo(IV)  $3d_{5/2}$ , Mo(IV)  $3d_{3/2}$ , Mo(V)  $3d_{5/2}$  and Mo(V)  $3d_{3/2}$ , respectively [22, 36]. When charged to 3 V, the peaks at 710.8 and 723.9 eV (Fig. S9(c) in the ESM) are related to  $\text{Fe}^{2+}$  [35], indicating that the Fe nanoparticles are oxidized to  $\text{Fe}^{2+}$ . Two strong satellite peaks, which appear at 715.9 and 729 eV,

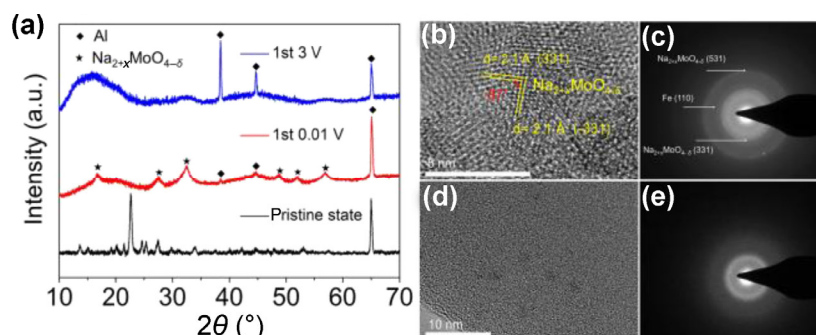


**Figure 5** Sodium-storage mechanism of FMO: (a) *ex-situ* XRD patterns of FMO in different states; (b) HRTEM and (c) selected area electron diffraction (SAED) images of FMO in the fully discharged state; (d) HRTEM and (e) SAED images of FMO in the fully charged state.

are ascribed to  $\text{Fe}^{2+}$  [37]. The Mo 3d XPS spectrum (Fig. S9(d) in the ESM) displays peaks at 230.8, 232.6, 233.9 and 235.7 eV, corresponding to Mo(V)  $3d_{5/2}$ , Mo(VI)  $3d_{5/2}$ , Mo(V)  $3d_{3/2}$ , and Mo(VI)  $3d_{3/2}$ , respectively [22, 36].

In brief, the superior rate capability and cycling performance of the graphene oxide-decorated  $\text{Fe}_2(\text{MoO}_4)_3$  microflowers in lithium and sodium storage can be attributed to the following aspects: (1) the 3D microflowers structure composed of nanosheets is beneficial for the ion transport and volume-change accommodation during cycling; (2) the GO improves the electrical conductivity of the electrode, which provides fast electrochemical kinetics; (3) the GO can effectively maintain the morphology and restrain pulverization of the electrode materials.

## 4 Conclusions

In summary, graphene oxide-decorated  $\text{Fe}_2(\text{MoO}_4)_3$  microflowers were fabricated by a facile one-step water-bath synthesis. Owing to the introduction of GO, the FMO/GO composite displays enhanced electrochemical performance. For lithium storage, the FMO/GO delivers a high discharge capacity of  $1,220 \text{ mAh}\cdot\text{g}^{-1}$  after 50 cycles at  $200 \text{ mA}\cdot\text{g}^{-1}$ , and  $685 \text{ mAh}\cdot\text{g}^{-1}$  at  $10 \text{ A}\cdot\text{g}^{-1}$ . For sodium storage, the FMO/GO delivers a discharge capacity of  $571 \text{ mAh}\cdot\text{g}^{-1}$ , retaining  $307 \text{ mAh}\cdot\text{g}^{-1}$  after 100 cycles. The possible sodium storage mechanism of FMO was investigated by *ex-situ* XRD, HRTEM, SAED, and XPS analysis. The results indicate that the FMO/GO composite is a promising anode material for LIBs and SIBs.

## Acknowledgements

This work was supported by the National Key Research and Development Program of China (No. 2016YFA0202603), the National Basic Research Program of China (No. 2013CB934103), the Programme of Introducing Talents of Discipline to Universities (No. B17034), the National Natural Science Foundation of China (Nos. 51521001, 21673171, 51502226, and 51302203), the National Natural Science Fund for Distinguished Young Scholars (No. 51425204), and the Fundamental Research Funds for the Central Universities (WUT: 2016III001, 2016III002, 2016III006).

Thanks to Prof. Zhaoping Liu and Prof. Xufeng Zhou at Ningbo Institute of Material Technology and Engineering of Chinese Academy of Sciences for providing the graphene oxide. Prof. Liqiang Mai gratefully acknowledged financial support from China Scholarship Council (No. 201606955096).

**Electronic Supplementary Material:** Supplementary material (Raman spectra of FMO/GO, GO; TG curve of FMO/GO; SEM images of FMO/GO; SEM and TEM images of FMO; the long-term cycling performance of FMO/GO at  $1 \text{ A}\cdot\text{g}^{-1}$  in LIBs; Nyquist plots of FMO and FMO/GO in lithium storage; Nyquist plots of FMO and FMO/GO in sodium storage; SEM images of FMO and FMO/GO after 50 cycles in sodium storage; XPS spectra of FMO; comparison of the results in this study with reported performance of transition metal molydbates in lithium storage; comparison of the results in this study with reported performance of transition metal molydbates in sodium storage) is available in the online version of this article at <https://doi.org/10.1007/s12274-017-1742-9>.

## References

- [1] Goodenough, J. B.; Kim, Y. Challenges for rechargeable Li batteries. *Chem. Mater.* **2010**, *22*, 587–603.
- [2] Armand, M.; Tarascon, J. M. Building better batteries. *Nature* **2008**, *451*, 652–657.
- [3] Larcher, D.; Tarascon, J. M. Towards greener and more sustainable batteries for electrical energy storage. *Nat. Chem.* **2015**, *7*, 19–29.
- [4] Mai, L. Q.; Tian, X. C.; Xu, X.; Chang, L.; Xu, L. Nanowire electrodes for electrochemical energy storage devices. *Chem. Rev.* **2014**, *114*, 11828–11862.
- [5] Ren, H.; Sun, J. J.; Yu, R. B.; Yang, M.; Gu, L.; Liu, P. R.; Zhao, H. J.; Kisailus, D.; Wang, D. Controllable synthesis of mesostructures from  $\text{TiO}_2$  hollow to porous nanospheres with superior rate performance for lithium ion batteries. *Chem. Sci.* **2016**, *7*, 793–798.
- [6] Zhang, J.; Ren, H.; Wang, J. Y.; Qi, J.; Yu, R. B.; Wang, D.; Liu, Y. L. Engineering of multi-shelled  $\text{SnO}_2$  hollow microspheres for highly stable lithium-ion batteries. *J. Mater. Chem. A* **2016**, *4*, 17673–17677.
- [7] Lai, X. Y.; Halpert, J. E.; Wang, D. Recent advances in micro-/nano-structured hollow spheres for energy applications: From simple to complex systems. *Energy Environ. Sci.* **2012**, *5*, 5604–5618.

- [8] Wang, J. Y.; Tang, H. J.; Zhang, L. J.; Ren, H.; Yu, R. B.; Jin, Q.; Qi, J.; Mao, D.; Yang, M.; Wang, Y. et al. Multi-shelled metal oxides prepared via an anion-adsorption mechanism for lithium-ion batteries. *Nat. Energy* **2016**, *1*, 16050.
- [9] Kang, B.; Ceder, G. Battery materials for ultrafast charging and discharging. *Nature* **2009**, *458*, 190–193.
- [10] Luo, C.; Xu, Y. H.; Zhu, Y. J.; Liu, Y. H.; Zheng, S. Y.; Liu, Y.; Langrock, A.; Wang, C. S. Selenium@ mesoporous carbon composite with superior lithium and sodium storage capacity. *ACS Nano* **2013**, *7*, 8003–8010.
- [11] Yabuuchi, N.; Kubota, K.; Dahbi, M.; Komaba, S. Research development on sodium-ion batteries. *Chem. Rev.* **2014**, *114*, 11636–11682.
- [12] Kundu, D.; Talaie, E.; Duffort, V.; Nazar, L. F. The emerging chemistry of sodium ion batteries for electrochemical energy storage. *Angew. Chem., Int. Ed.* **2015**, *54*, 3431–3448.
- [13] Liu, Y. C.; Zhang, N.; Yu, C. M.; Jiao, L. F.; Chen, J. MnFe<sub>2</sub>O<sub>4</sub>@C nanofibers as high-performance anode for sodium-ion batteries. *Nano Lett.* **2016**, *16*, 3321–3328.
- [14] Li, Q. D.; Wei, Q. L.; Zuo, W. B.; Huang, L.; Luo, W.; An, Q. Y.; Pelenovich, V. O.; Mai, L. Q.; Zhang, Q. J. Greigite Fe<sub>3</sub>S<sub>4</sub> as a new anode material for high-performance sodium-ion batteries. *Chem. Sci.* **2017**, *8*, 160–164.
- [15] Kim, S. W.; Seo, D. H.; Ma, X. H.; Ceder, G.; Kang, K. Electrode materials for rechargeable sodium-ion batteries: Potential alternatives to current lithium-ion batteries. *Adv. Energy Mater.* **2012**, *2*, 710–721.
- [16] Stevens, D. A.; Dahn, J. R. The mechanisms of lithium and sodium insertion in carbon materials. *J. Electrochem. Soc.* **2001**, *148*, A803–A811.
- [17] Zhao, Y.; Li, X. F.; Yan, B.; Xiong, D. B.; Li, D. J.; Lawes, S.; Sun, X. L. Recent developments and understanding of novel mixed transition-metal oxides as anodes in lithium ion batteries. *Adv. Energy Mater.* **2016**, *6*, 1502175.
- [18] Pramanik, A.; Maiti, S.; Mahanty, S. Superior lithium storage properties of Fe<sub>2</sub>(MoO<sub>4</sub>)<sub>3</sub>/MWCNT composite with a nanoparticle (0D)-nanorod (1D) hetero-dimensional morphology. *Chem. Eng. J.* **2017**, *307*, 239–248.
- [19] Wang, B.; Li, S. M.; Wu, X. Y.; Tian, W. M.; Liu, J. H.; Yu, M. Integration of network-like porous NiMoO<sub>4</sub> nano-architectures assembled with ultrathin mesoporous nanosheets on three-dimensional graphene foam for highly reversible lithium storage. *J. Mater. Chem. A* **2015**, *3*, 13691–13698.
- [20] Yao, J. Y.; Gong, Y. J.; Yang, S. B.; Xiao, P.; Zhang, Y. H.; Keyshar, K.; Ye, G. L.; Ozden, S.; Vajtai, R.; Ajayan, P. M. CoMoO<sub>4</sub> nanoparticles anchored on reduced graphene oxide nanocomposites as anodes for long-life lithium-ion batteries. *ACS Appl. Mater. Interfaces* **2014**, *6*, 20414–20422.
- [21] Guan, B. Q.; Sun, W. W.; Wang, Y. Carbon-coated MnMoO<sub>4</sub> nanorod for high-performance lithium-ion batteries. *Electrochim. Acta* **2016**, *190*, 354–359.
- [22] Chen, N.; Gao, Y.; Zhang, M. N.; Meng, X.; Wang, C. Z.; Wei, Y. J.; Du, F.; Chen, G. Electrochemical properties and sodium-storage mechanism of Ag<sub>2</sub>Mo<sub>2</sub>O<sub>7</sub> as the anode material for sodium-ion batteries. *Chem.–Eur. J.* **2016**, *22*, 7248–7254.
- [23] Sheng, J. Z.; Zang, H.; Tang, C. J.; An, Q. Y.; Wei, Q. L.; Zhang, G. B.; Chen, L. N.; Peng, C.; Mai, L. Q. Graphene wrapped NASICON-type Fe<sub>2</sub>(MoO<sub>4</sub>)<sub>3</sub> nanoparticles as a ultra-high rate cathode for sodium ion batteries. *Nano Energy* **2016**, *24*, 130–138.
- [24] Yang, T.; Zhang, H. N.; Luo, Y. Z.; Mei, L.; Guo, D.; Li, Q. H.; Wang, T. H. Enhanced electrochemical performance of CoMoO<sub>4</sub> nanorods/reduced graphene oxide as anode material for lithium-ion batteries. *Electrochim. Acta* **2015**, *158*, 327–332.
- [25] Li, Q. D.; Wei, Q. L.; Sheng, J. Z.; Yan, M. Y.; Zhou, L.; Luo, W.; Sun, R. M.; Mai, L. Q. Mesoporous Li<sub>3</sub>VO<sub>4</sub>/C submicron-ellipsoids supported on reduced graphene oxide as practical anode for high-power lithium-ion batteries. *Adv. Sci.* **2015**, *2*, 1500284.
- [26] Mai, L. Q.; Wei, Q. L.; An, Q. Y.; Tian, X. C.; Zhao, Y. L.; Xu, X.; Xu, L.; Chang, L.; Zhang, Q. J. Nanoscroll buffered hybrid nanostructural VO<sub>2</sub> (B) cathodes for high-rate and long-life lithium storage. *Adv. Mater.* **2013**, *25*, 2969–2973.
- [27] Yue, J. L.; Zhou, Y. N.; Shi, S. Q.; Shadik, Z.; Huang, X. Q.; Luo, J.; Yang, Z. Z.; Li, H.; Gu, L.; Yang, X. Q. et al. Discrete Li-occupation versus pseudo-continuous Na-occupation and their relationship with structural change behaviors in Fe<sub>2</sub>(MoO<sub>4</sub>)<sub>3</sub>. *Sci. Rep.* **2015**, *5*, 8810.
- [28] Zheng, H.; Wang, S. Q.; Wang, J. Z.; Wang, J.; Li, L.; Yang, Y.; Feng, C. Q.; Sun, Z. Q. 3D Fe<sub>2</sub>(MoO<sub>4</sub>)<sub>3</sub> microspheres with nanosheet constituents as high-capacity anode materials for lithium-ion batteries. *J. Nanopart. Res.* **2015**, *17*, 449.
- [29] Reddy, M. V.; Yu, T.; Sow, C. H.; Shen, Z. X.; Lim, C. T.; Rao, G. V. S.; Chowdari, B. V. R. α-Fe<sub>2</sub>O<sub>3</sub> nanoflakes as an anode material for Li-ion batteries. *Adv. Funct. Mater.* **2007**, *17*, 2792–2799.
- [30] Wu, Z. G.; Zhong, Y. J.; Liu, J.; Wu, J. H.; Guo, X. D.; Zhong, B. H.; Zhang, Z. Y. Subunits controlled synthesis of α-Fe<sub>2</sub>O<sub>3</sub> multi-shelled core-shell microspheres and their effects on lithium/sodium ion battery performances. *J. Mater. Chem. A* **2015**, *3*, 10092–10099.
- [31] Cai, Z. Y.; Xu, L.; Yan, M. Y.; Han, C. H.; He, L.; Hercule, K. M.; Niu, C. J.; Yuan, Z. F.; Xu, W. W.; Qu, L. B. et al. Manganese oxide/carbon yolk-shell nanorod anodes for high capacity lithium batteries. *Nano Lett.* **2015**, *15*, 738–744.

- [32] Li, H.; Ma, H. R.; Yang, M.; Wang, B.; Shao, H.; Wang, L.; Yu, R. B.; Wang, D. Highly controlled synthesis of multi-shelled NiO hollow microspheres for enhanced lithium storage properties. *Mater. Res. Bull.* **2017**, *87*, 224–229.
- [33] Luo, W.; Calas, A.; Tang, C. J.; Li, F.; Zhou, L.; Mai, L. Q. Ultralong Sb<sub>2</sub>Se<sub>3</sub> nanowire-based free-standing membrane anode for lithium/sodium ion batteries. *ACS Appl. Mater. Interfaces* **2016**, *8*, 35219–35226.
- [34] Li, X. Q.; Zhang, W. X. Sequestration of metal cations with zerovalent iron nanoparticles—a study with high resolution X-ray photoelectron spectroscopy (HR-XPS). *J. Phys. Chem. C* **2007**, *111*, 6939–6946.
- [35] Yamashita, T.; Hayes, P. Analysis of XPS spectra of Fe<sup>2+</sup> and Fe<sup>3+</sup> ions in oxide materials. *Appl. Surf. Sci.* **2008**, *254*, 2441–2449.
- [36] Światowska-Mrowiecka, J.; de Diesbach, S.; Maurice, V.; Zanna, S.; Klein, L.; Briand, E.; Vickridge, I.; Marcus, P. Li-ion intercalation in thermal oxide thin films of MoO<sub>3</sub> as studied by XPS, RBS, and NRA. *J. Phys. Chem. C* **2008**, *112*, 11050–11058.
- [37] Grosvenor, A. P.; Kobe, B. A.; Biesinger, M. C.; McIntyre, N. S. Investigation of multiplet splitting of Fe 2p XPS spectra and bonding in iron compounds. *Surf. Interface Anal.* **2004**, *36*, 1564–1574.